GEOPHYSICS, VOL. 88, NO. 4 (JULY-AUGUST 2023); P. KS101–KS112, 17 FIGS., 1 TABLE.
10.1190/GEO2022-0445.1

Geotechnical site characterization with 3D ambient noise tomography

Yao Wang[1], Khiem T. Tran[1], Brady R. Cox[2], and Joseph P. Vantassel[3]

ABSTRACT

We develop a new 3D ambient noise tomography (3D ANT) method for geotechnical site characterization. It requires recording ambient noise fields using a 2D surface array of geophones, from which experimental crosscorrelation functions (CCFs) are then extracted and directly inverted to obtain an S-wave velocity (V_S) structure. The method consists of a forward simulation using 3D P-SV elastic wave equations to compute the synthetic CCF and an adjoint-state inversion to match the synthetic CCFs to the experimental CCFs for extraction of V_S. The main advantage of the presented method, as compared with conventional passive-source seismic methods using characteristics of Green's function (GF), is that it does not require equal energy on both sides of each receiver pair or far-field wavefields to retrieve the true GF. Instead, the source power spectrum density is inverted during the analysis and incorporated into the forward simulation of the synthetic CCFs to account for source energy distribution. After testing on synthetic data, the 3D ANT method is applied to 3 h of ambient noise recordings at the Garner Valley Downhole Array (GVDA) site in California, using a surface array of 196 geophones placed on a 14 × 14 grid with 5 m spacing. The inverted 3D V_S model is found to be consistent with previous invasive and noninvasive geotechnical characterization efforts at the GVDA site.

INTRODUCTION

Active-source seismic methods such as multichannel analysis of surface waves (MASW) and full-waveform inversion (FWI) have become efficient tools for geotechnical site characterization (Park et al., 1999; Tran et al., 2013; Tran and Sperry, 2018; Nguyen and Tran, 2018; Alam, 2019; Alam and Shukla, 2020; Mirzanejad et al., 2020). Although these methods can provide accurate subsurface profiles, they require low-frequency energy (<10 Hz) for deep investigations (>20 m in depth) (Mirzanejad et al., 2021). As large, powerful active sources capable of generating such low-frequency energy are expensive and generally not available for use on most projects, many have sought to take advantage of the low-frequency ambient noise already present in the environment for deep site characterization. Existing ambient noise methods can be categorized into three groups, as detailed next.

The first group is surface wave methods. With the popularization of linear array active-source surface wave methods (e.g., MASW; Park et al., 1999; Xia et al., 1999), researchers began investigating if linear arrays also could be used to measure ambient noise to derive deep 1D V_S models (e.g., ReMi^{TM}; Louie, 2001). Although linear array ambient noise methods have been widely used in practice due to their simplicity, the engineering research community generally agrees that 2D arrays should be used for ambient noise testing whenever possible (Foti et al., 2018). Ambient noise measurements made with 2D arrays have shown that many sites (rural and urban) have clear passive energy arrival directions and that those arrival directions often vary as a function of frequency (Tokimatsu, 1997; Di Giulio et al., 2006; Rosenblad and Li, 2009; Endrun et al., 2010). These variations are problematic for linear array methods because the direction of ambient noise wave arrivals cannot be determined (Cox and Beekman, 2011). Thus, 2D surface arrays are essential for ambient noise measurements.

Surface wave methods based on ambient noise measurements from 2D arrays require complex array-processing techniques, of which there are two main types: frequency-wavenumber (*f*-*k*) beamforming and spatial autocorrelation (SPAC). The *f*-*k*-type methods were first introduced by Lacoss et al. (1969). However, numerous others have adjusted the initial formulation (e.g., Capon, 1969; Nolet and Panza, 1976; Johnson and Dudgeon, 1993). In general, *f*-*k*-type methods use beamforming techniques to determine the direction and speed of incoming ambient noise as a function of frequency. The phase

Manuscript received by the Editor 7 July 2022; revised manuscript received 21 February 2023; published ahead of production 28 March 2023; published online 23 May 2023.

[1]University of Florida, Department of Civil and Coastal Engineering, Gainesville, Florida, USA. E-mail: wangyao@ufl.edu; ttk@ufl.edu (corresponding author).
[2]Utah State University, Department of Civil and Environmental Engineering, Logan, Utah, USA. E-mail: brady.cox@usu.edu.
[3]Virginia Polytechnic Institute and State University, Department of Civil and Environmental Engineering, Blacksburg, Virginia, USA. E-mail: jpvantassel@vt.edu.

velocity and frequency of these incoming waves represent the dispersion characteristics of the site, which can be inverted for 1D V_S of the subsurface (e.g., Cox and Teague, 2016; Teague et al., 2018; Vantassel et al., 2018). SPAC-type methods (e.g., Aki, 1957; Henstridge, 1979; Asten et al., 2002; Okada, 2003; Cho et al., 2004; Foti et al., 2018; Hayashi et al., 2022) also have been used successfully to develop deep 1D V_S profiles from ambient noise recordings. However, they do not require determining the frequency-dependent direction of ambient noise propagation but instead rely on the assumption of a relatively homogeneous azimuthal distribution of incoming wavefield energy. The *f*-*k*-type methods have the advantage of being able to accurately process ambient wavefields with distinct arrival directions when the wavefield energy is relatively homogeneous in all azimuths. Importantly, all surface wave methods (*f*-*k* type and SPAC type) are only capable of providing 1D V_S profiles that represent an average over the volume of material beneath the receiver array within a depth of approximately one wavelength for each frequency.

The second group of ambient noise methods uses traveltime or dispersion characteristics of Green's functions (GFs), which are calculated by crosscorrelating long noise records between pairs of receivers located within either a linear or 2D array. Methods using the traveltime of the GFs, such as tomographic methods (Barmin et al., 2001) and eikonal tomography (Lin et al., 2009), have been used to obtain 2D maps of frequency-dependent group or phase velocity at regional and continental scales around the world (e.g., United States: Ekström et al., 2009; Lin et al., 2013; Europe: Ritzwoller et al., 2011; Schippkus et al., 2018; and Asia: Fang et al., 2010; Das and Rai, 2016). Although these methods produce large-scale 2D velocity models, the velocities are averaged over large spatial distances/depths, thus resulting in limited resolution.

For the methods using the dispersion characteristics of GFs, the Rayleigh or Love wave dispersion data at each grid location between a pair of receivers are inverted for a 1D V_S profile beneath that location. These 1D V_S profiles are then stitched together to create pseudo-2D/3D models of V_S. Such studies also have been performed at regional (<1 km) and continental (>1 km) scales (e.g., United States: Moschetti et al., 2010; Yang et al., 2011; Europe: Behm et al., 2016; and Asia: Guo et al., 2009; Zheng et al., 2010). Similar to the surface wave approach, these methods average V_S over the volume of material beneath the distance between a pair of receivers and within a depth of approximately one wavelength for each frequency. Thus, they are also inherently one dimensional and do not provide V_S cell-by-cell.

The third group of ambient noise methods uses FWI of crosscorrelation functions (CCFs) of noise fields. Toward the FWI of CCFs, structural and source kernels were first derived by Tromp et al. (2010). The practical field applications have predominantly been conducted at global and local scales (De Ridder and Maddison, 2018; Sager et al., 2018). At engineering scales (<50 m depth), 2D ambient noise tomography (2D ANT) (Wang et al., 2021) has recently been developed. The 2D ANT method was able to invert CCFs of predominantly traffic noise to extract a 2D V_S model to detect roadway sinkholes. Building on the 2D ANT method, this study develops a new 3D ANT method to directly invert CCFs of ambient noise fields for extraction of a 3D V_S model. Addressing the main issue of unknown noise sources, the source power spectrum density (PSD) is inverted and used for the forward simulation of synthetic CCFs. The 3D ANT methodology is derived here, and its capabilities are evaluated with synthetic and field data sets.

METHODOLOGY

The presented 3D ANT method consists of a forward simulation to compute the synthetic CCF and an adjoint-state inversion to match the simulated CCFs to the observed CCFs for extraction of subsurface structures. The 3D P-SV elastic wave equations and their numerical solutions (Nguyen and Tran, 2018) are used to simulate the noise wavefields and GFs required for computing the synthetic CCF during inversion, as discussed in the following sections.

Forward simulation

The CCF $C^{\alpha\beta}$ between the two signals s^α and s^β is explicitly given by

$$C^{\alpha\beta}(t) = \int s^\alpha(\tau) s^\beta(t+\tau) d\tau, \tag{1}$$

where variables α and β are the position indexes of the receiver stations, t denotes the time, and τ is the time offset. Equation 1 requires performing the forward simulation for each source location individually to obtain seismograms s^α and s^β. However, it is not possible to explicitly simulate the seismograms due to a large number of sources contributing to the noise wavefield with unknown locations. Thus, we adopt the implicit approach (Sager et al., 2018, 2020; Wang et al., 2021) to compute the CCF. The CCF can be formulated via GFs as

$$\begin{aligned} C^{\alpha\beta}(t) = \frac{1}{2\pi}\int\int_{\Omega''}\int_{\Omega'} G(\mathbf{x}^\alpha,\mathbf{x}',\omega) f(\mathbf{x}',\omega) G^*(\mathbf{x}^\beta,\mathbf{x}'',\omega) \\ f^*(\mathbf{x}'',\omega)\exp(i\omega t) d\Omega' d\Omega'' d\omega, \end{aligned} \tag{2}$$

where ω is the angular frequency, i is the imaginary unit, and the asterisk symbol denotes the complex conjugate. Variables $\mathbf{x}'$ and $\mathbf{x}''$ are the two arbitrary locations in the 3D domain Ω, integrals $\int_{\Omega'} d\Omega'$ and $\int_{\Omega''} d\Omega''$ denote the integration over domain Ω twice, distinctively, $G(\mathbf{x}^\alpha, \mathbf{x}, t)$ is the GF with the source located at $\mathbf{x}^\alpha$, and $f(\mathbf{x}, t)$ is the source function. Assuming that the spatial correlation length of noise sources is shorter than the seismic wavelengths present in the noise, the source terms can be approximated with a delta function (δ) in space and the source PSD $S(\mathbf{x}, \omega)$ (Wapenaar, 2004; Wapenaar and Fokkema, 2006):

$$f(\mathbf{x}',\omega) f^*(\mathbf{x}'',\omega) = S(\mathbf{x}',\omega)\delta(\mathbf{x}'-\mathbf{x}''). \tag{3}$$

By its definition, the PSD is a field of scalar values that show the spatial location and the strength of the sources. With this approximation, equation 2 becomes

$$\begin{aligned} & C^{\alpha\beta}(t) \\ & = \frac{1}{2\pi}\int\int_{\Omega} G(\mathbf{x}^\alpha,\mathbf{x},\omega)[G^*(\mathbf{x}^\beta,\mathbf{x},\omega)S(\mathbf{x},\omega)]\exp(i\omega t) d\mathbf{x} d\omega \end{aligned} \tag{4}$$

and

$$C^{\alpha\beta}(\omega) = \int_{\Omega} G(\mathbf{x}^{\alpha}, \mathbf{x}, \omega)[G^{*}(\mathbf{x}^{\beta}, \mathbf{x}, \omega)S(\mathbf{x}, \omega)]d\mathbf{x}. \quad (5)$$

Equations 4 and 5 can be used to compute the CCF in the time and frequency domains, respectively. Because the locations of the individual noise sources cannot be determined for an explicit computation, the CCF is computed implicitly based on the noise source distribution (all noise events) via equation 5. We compute the CCF between $\mathbf{x}^{\alpha}$ and $\mathbf{x}^{\beta}$ by performing the following steps:

1) Run two forward 3D wavefield propagation simulations to compute the GFs $G(\mathbf{x}^{\alpha}, \mathbf{x}, \omega)$ and $G(\mathbf{x}^{\beta}, \mathbf{x}, \omega)$ with sources at $\mathbf{x}^{\alpha}$ and $\mathbf{x}^{\beta}$.
2) Multiply $G(\mathbf{x}^{\alpha}, \mathbf{x}, \omega)$ with the complex conjugate $G^{*}(\mathbf{x}^{\beta}, \mathbf{x}, \omega)$ and the noise source PSD $S(\mathbf{x}, \omega)$. In this study, the noise source PSD is inverted from measured CCFs (either synthetic or experimental) in the time domain as an equivalent (average) source distribution for all frequencies within a filtering band. It represents the relative spatial distribution of source energy (e.g., $S(\mathbf{x}, \omega) = 0$ if there is no source and 1 if there is a source with the highest energy at $\mathbf{x}$ location). Here, $S(\mathbf{x}, \omega)$ is taken as the inverted PSD, which is the same for all frequencies within the filtering band. This approach works for synthetic and field experiments.
3) Sum over all grid points (integration over space $\mathbf{x}$).
4) Transform the frequency-domain CCF to the time domain.

Adjoint-state inversion

The inversion process minimizes the misfit between the observed and the simulated CCFs to extract the subsurface velocity structures. We define the misfit (residual) between the observed and synthetic CCFs as

$$\delta C = C_{\text{obs}} - C_{\text{syn}}. \quad (6)$$

The objective function (E) is then defined as the $L2$ norm of the misfit:

$$E = \frac{1}{2}\delta C^{\mathrm{T}}\delta C = \frac{1}{2}\sum_{\alpha}\int dt \sum_{\beta}\delta C^{2}. \quad (7)$$

To optimize the objective function, we analyze the three main components that produce the misfit of CCFs. They are the source signature (the source time function), the source PSD, and the geologic structure (the S-wave velocity V_{S}, P-wave velocity V_{P}, and mass density ρ). The source signature governs the shape of the CCF waveforms, the PSD defines the location and strength of the noise sources, and the geologic structure influences the CCFs waveform shape and amplitude. Among these three components, the source time function estimation is relatively straightforward, as it can be implemented independently of the geologic structure. We do so in this work using the deconvolution method proposed by Wang et al., (2021). To address the remaining two components, we invert the PSD and V_{S} using the sensitivity kernels developed by Sager et al. (2020).

To update the spatial component of the PSD distribution, we first use the adjoint technique to calculate the PSD kernel (Sager et al., 2020):

$$K_{s}(x) = -\sum_{\alpha=1}^{n}\int u^{\dagger}(\mathbf{x})[G^{*}(\alpha, x)S(x)]d\omega, \quad (8)$$

where $u^{\dagger}$ is the adjoint wavefield and $G^{*}(\alpha, x)S(x)$ is the broadcast wavefield of the forward-propagating wavefield recorded at any area where the PSD is positive (where a source exists). This means using the recorded wavefield as a distributed source signal for the simulation of the adjoint wavefield. The frequency-domain multiplication is implemented by a time-domain convolution (zero-lag crosscorrelation). We implemented this calculation in the time domain because of our available time-domain solution of 3D P-SV elastic wave equations (Nguyen and Tran, 2018).

Next, the geologic structure refers to an earth model vector $\mathbf{m}(\mathbf{x})$, which characterizes the subsurface material properties $(V_{\mathrm{P}}, V_{\mathrm{S}}, \rho)$. The vector $\mathbf{m}(\mathbf{x})$ controls the GFs in the forward simulation equations 4 and 5. To derive the kernel, we use the elastic wavefield modeling operator as $\mathcal{L}(\circ)$, where $\circ$ is a placeholder. With this operator, $\mathcal{L}(u(x))$ represents the forward elastic wavefield simulation in terms of displacement vector $\mathbf{u}(\mathbf{x})$. The time-domain finite-difference implementation of $\mathcal{L}(\circ)$ (Nguyen and Tran, 2018) is used for wavefield simulation throughout this work. The geologic structure kernel with respect to $\mathbf{m}(\mathbf{x})$ is computed as (Sager et al., 2020)

$$K_{m}(x) = \sum_{\alpha=1}^{n}\int [u^{\dagger}(\mathbf{x})\mathcal{L}(C(\mathbf{x}, \alpha)) + C_{\alpha}^{\dagger}(\mathbf{x})\mathcal{L}(G(\mathbf{x}, \alpha))]dt. \quad (9)$$

For the first part inside the square bracket, the adjoint wavefield $u^{\dagger}(\mathbf{x})$ is numerically computed by injecting the CCF residuals (equation 6) at the receiver locations. At each reference station α, the residual δC_{α} consists of n channels, which are backward propagated simultaneously to generate wavefield $u^{\dagger}$. The operation $\mathcal{L}(C(\mathbf{x}, \alpha))$ denotes the correlation wavefield that propagates from the noise source to the receivers. To calculate this wavefield, we first inject the source time function at the reference station α and record the forward-propagating wavefield at any area where there is a noise source (with a PSD magnitude > 0). We then do another forward simulation to broadcast the recorded wavefield by multiplying the broadcast wavefield with the PSD to produce the correlation wavefield $\mathcal{L}(C(\mathbf{x}, \alpha))$.

For the second part inside the square bracket of equation 9, $C_{\alpha}^{\dagger}$ denotes the adjoint CCF residual wavefield. It is calculated by

$$C_{\alpha}^{\dagger}(x) = \int G_{\alpha}^{*}(x, t)[u^{\dagger *}(x)S(x)]dt. \quad (10)$$

To compute this wavefield, we perform a forward simulation to backward propagate the CCF residuals δC and record the wavefield at any area with a noise source (PSD > 0). Then, we do another forward simulation to broadcast the recorded CCF residual wavefield and multiply the broadcast wavefield with the PSD to obtain the adjoint CCF residual wavefield $C_{\alpha}^{\dagger}(x)$. The computing of $\mathcal{L}(G(\mathbf{x}, \alpha))$ is done by injecting the source time function at station

α and recording the forward-propagating wavefield. Similar to the first part in the square bracket of equation 9, the second part is calculated by performing time-domain convolution of $C_{\alpha}^{\dagger}(x)$ and $\mathcal{L}(G(\mathbf{x},\alpha))$.

More specifically, we formulate and compute the gradients for Lamé parameters λ and μ using strains (ε) of the simulated wavefields as

$$\delta\lambda = \int_0^T \{(\varepsilon_x + \varepsilon_y + \varepsilon_z)(\varepsilon_x^{c+} + \varepsilon_y^{c+} + \varepsilon_z^{c+})$$
$$+ (\varepsilon_x^{+} + \varepsilon_y^{+} + \varepsilon_z^{+})(\varepsilon_x^{c} + \varepsilon_y^{c} + \varepsilon_z^{c})\}dt,$$
$$\delta\lambda = \int_0^T \{(\varepsilon_x\varepsilon_x^{c+} + \varepsilon_y\varepsilon_y^{c+} + \varepsilon_z\varepsilon_z^{c+}) + (\varepsilon_{xy} + \varepsilon_{yx})(\varepsilon_{xy}^{c+} + \varepsilon_{yx}^{c+})$$
$$+ (\varepsilon_{yz} + \varepsilon_{zy})(\varepsilon_{yz}^{c+} + \varepsilon_{zy}^{c+}) + (\varepsilon_{zx} + \varepsilon_{xz})(\varepsilon_{zx}^{c+} + \varepsilon_{xz}^{c+})$$
$$+ (\varepsilon_x^{c}\varepsilon_x^{+} + \varepsilon_y^{c}\varepsilon_y^{+} + \varepsilon_z^{c}\varepsilon_z^{+})(\varepsilon_{xy}^{c} + \varepsilon_{yx}^{c})(\varepsilon_{xy}^{+} + \varepsilon_{yx}^{+})$$
$$+ (\varepsilon_{yz}^{c} + \varepsilon_{zy}^{c})(\varepsilon_{yz}^{+} + \varepsilon_{zy}^{+}) + (\varepsilon_{zx}^{c} + \varepsilon_{xz}^{c})(\varepsilon_{zx}^{+} + \varepsilon_{xz}^{+})\}dt. \quad (11)$$

The strain tensor $\boldsymbol{\varepsilon}$ is computed via the particle displacement $\mathbf{u}$ as $\boldsymbol{\varepsilon}_{ij} = 1/2((\partial\mathbf{u}_i/\partial x_j) + (\partial\mathbf{u}_j/\partial x_i))$. Notation ε is the strain of the forward-propagating wavefield $\mathcal{L}(G(\mathbf{x},\alpha))$, ε^{+} is the strain of the adjoint wavefields $u^{\dagger}$, ε^{c} is the strain of the propagating correlation wavefields $\mathcal{L}(C(\mathbf{x},\alpha))$, and ε^{c+} is the strain of the adjoint correlation wavefield $C^{\dagger}$. Based on the elastic relationships among variables V_S, λ, μ, and ρ, the gradient with respect to V_S can be written as

$$\delta V_S = -4\rho V_S \delta\lambda + 2\rho V_S \delta\mu. \quad (12)$$

Finally, the PSD and V_S are updated iteratively by

$$\begin{cases} S^{p+1} = \|S^p + \theta_1 |K_s|_{L1}\| \\ V_S^{p+1} = V_S^p + \theta_2 \delta V_S \end{cases}, \quad (13)$$

where the index p denotes the iteration number. The PSD kernel K_s is calculated in equation 8. The operator $|\circ|_{L1}$ is the $L1$ normalization. The operator $\|\circ\|$ denotes a PSD magnitude normalization. This normalization neglects the negative values and maps the nonnegative magnitude of the PSD to the range [0,1]. The step lengths θ_1 and θ_2 are positive scalars. The gradient δV_S is normalized by dividing its maximum magnitude. In this study, we use θ_1 equal to 0.05 (5% of the maximum normalized PSD) and θ_2 equal to 0.02 (2% of the maximum V_S of the current model during inversion).

SYNTHETIC EXPERIMENT

To validate the 3D ANT algorithm, we first test it with a 3D synthetic example. The synthetic model (Figure 1) is 160 m × 160 m × 45 m ($x \times y \times z$). It consists of a hypothetical soil profile with V_S that increases with depth and an embedded low-V_S anomaly at the center. The background velocity model consists of a top layer (0–15 m) of V_S = 200 m/s and a bottom layer (25–50 m) of V_S = 450 m/s. This model was built based on P-S borehole logging (Steller, 1996) at the Garner Valley Downhole Array (GVDA) site used for the field experiment. Between these two layers, V_S increases gradually from 200 to 450 m/s. A large low-V_S (50 m/s) anomaly of 30 m diameter is at the model center (x = 80 m, y = 80 m, and z = 20 m). The anomaly considerably influences the propagation of the wavefields because of its location and size. The V_P model is generated from V_S by assuming a Poisson's ratio of 1/3 for typical soils (i.e., V_P = 2 V_S), and ρ is set to 1800 kg/m^3. The test configuration consists of 196 vertical surface receivers located on a grid of 14 × 14 at 5 m spacing. The 196-channel receiver array covers a square area of 65 m × 65 m above the anomaly. In the x- and y-directions, the first receiver is located within the synthetic domain at 50 m, and the last is located at 115 m. The black triangles shown in Figure 1a are the receivers that define the array's boundary.

Although the presented ANT method is valid for surface and in-depth sources (e.g., the PSD is nonzero at depths), we limit the synthetic test to traffic noise (surface sources) to be consistent with field data presented subsequently. The numerical solution of the 3D elastic wave equation was used to simulate traffic noise. Here, 200 source locations were randomly placed on the surface around the receiver array (i.e., no noise sources were assumed inside of the array). The red circles shown in Figure 1a denote the locations of noise sources on the free surface. Similar to the field data presented subsequently, there are more noise sources distributed between x = 0 and x = 50 m (e.g., along a road). This denser clustering of the sources means that wave propagation through the array is dominant along the x-direction. The synthetic noise wavefields were simulated and recorded for 300 s (5 min). Note that, unlike field data with relatively spare source events in time, the synthetic sources are applied consistently throughout the recording, thereby reducing the need for long recordings of simulated noise data. During this time, each noise source was triggered once randomly in time as a vertical point source on the free surface.

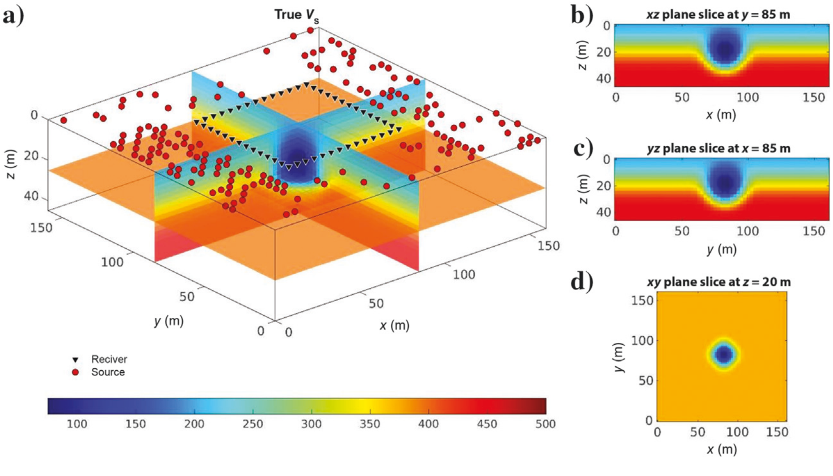

Figure 1. The true 3D V_S model for the synthetic example. (a) Red circles represent the sources. Black triangles represent the receivers on the array's boundary (note that 196 receivers are evenly distributed within this boundary on a 5 m grid — not shown). (b) The xz plane slice at y = 85 m, (c) yz plane slice at x = 85 m, and (d) xy plane slice at z = 20 m.

A Ricker wavelet of 5 Hz, with significant energy between 2 and 20 Hz, was used as the source signature for the forward simulation.

The synthetic noise signal, as recorded by all 196 receivers, is shown in Figure 2. These noise record traces are plotted against the station offset relative to the first receiver in the array (station 1). To extract the experimental CCFs, the 300 s long synthetic ambient noise record is divided into 300, 1 s time segments. Here, 1 s was selected to ensure that each surface event had sufficient time to travel through the entire test domain. A longer time segment can be used, but it may cause crosscorrelated wave events from different sources to be included in a single time segment, thereby reducing the quality of the computed CCFs. For each time segment, we calculate the CCF between every station pair using equation 1 and then stack the CCFs over time segments to obtain a 196-channel CCF data set. Here, we only show the CCFs relative to station 1, as shown in Figure 3. The 196 channels of the calculated CCF are sorted and depicted in time-sensor-number style in Figure 3a and offset-time style in Figure 3b. The offset-time style clearly shows the traveltime and the waveform change with distance.

Treating the experimental CCFs obtained from wave propagation simulations through the synthetic 3D model as the observations, we deploy the inversion method in an attempt to recover the true V_S structure and the PSD from a simple initial model. The initial V_S model (Figure 4) is laterally homogeneous with V_S increasing linearly as a function of depth from 200 to 500 m/s.

Although the CCFs are computed for surface (Rayleigh) and body waves and directly inverted, they represent the similarity between pairs of channels, and thus are dominated by surface waves (propagating horizontally from one channel to another). Compared with surface waves, reflected and refracted body waves are less correlated, and make less contribution to CCFs and inverted results. Due to the insensitivity of the Rayleigh-wave-dominated CCFs, our efforts to invert V_P and ρ have been unsuccessful. Therefore, we only invert V_S, while fixing ρ to its true value and updating V_P as twice the inverted V_S in this study.

The source time functions are estimated from the synthetic ambient noise records (i.e., CF observations) using the deconvolution method proposed by Wang et al. (2021). This method analyzes the signal autocorrelation at every reference station and aims to find a source time function $w(t)$ such that it minimizes an error E_{w_i} consisting of an $L2$ norm term and an $L1$ regularization term:

$$E_{wi} = \|\text{auto}(w(t)) - C_i(t)\|_{L2} + k_{\text{reg}}\|w(t)\|_{L1}, \tag{14}$$

where

$$\text{auto}(w(\tau)) = \int w(t+\tau)w(t)dt. \tag{15}$$

In equation 14, $C_i(t)$ is the noise autocorrelation at reference station i, and the coefficient k_{reg} is a regularization factor. This positive factor puts weight on the $L1$ norm of the time source function, which helps to reduce overfitting. Multiple values of k_{reg} between 1.0 and 10.0 were tested and k_{reg} of 2.0 produced the best results and, thus, 2.0 is used in this study. The source estimation was performed on the stacked CCFs for all 196 reference stations to obtain 196 source signatures, and the estimated source signatures were then used for the forward simulation during inversion.

In addition to the velocity structure, an accurate estimation of the PSD is important for a good match with the measured CCFs. To invert for the PSD, we start with a homogeneous source power spectrum (Figure 5a). Because of the assumption of no internal sources, the initial power spectrum has a value of one outside of the receiver array and a value of zero inside the array. The velocity model and PSD are updated throughout the gradient-based inversion process. For this example, we used 45 iterations (30 iterations to update V_S and 15 iterations to update PSD). The PSD updates are at iterations 1–5, 16–20, and 31–35. During a PSD update, the PSD kernel is calculated using the latest updated V_S model. The V_S update and the PSD update do not interfere, which means that one feature is updated during each iteration, whereas the other is fixed. The entire analysis took approximately 31 h on a workstation computer (32 cores of 3.46 GHz each and RAM of 1.0 TB).

The inverted PSD is shown in Figure 5b. The true locations of the sources are marked with red circles in Figure 5b. The inverted PSD resembles the true distribution of the sources. This result indicates that the noise power is more substantial (normalized amplitude > 0.5) in the area between $x = 0$ and $x = 50$ m and is relatively weaker (normalized amplitude < 0.5) in other areas. The main

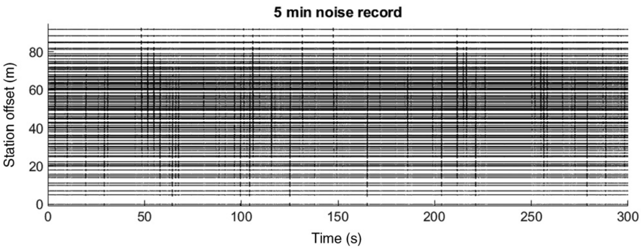

Figure 2. Simulated 5 min long noise record. The time series of ground motion is plotted against the station offset relative to station 1.

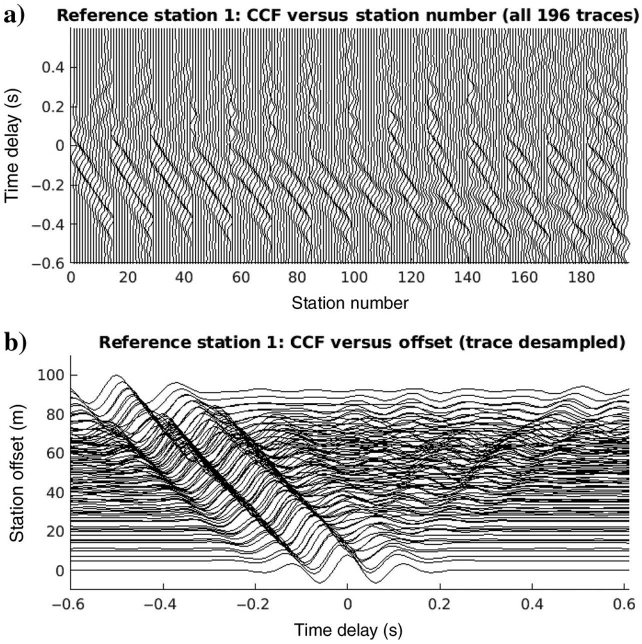

Figure 3. Calculated CCFs for the synthetic model displayed in (a) time-sensor-number style and (b) offset-time style.

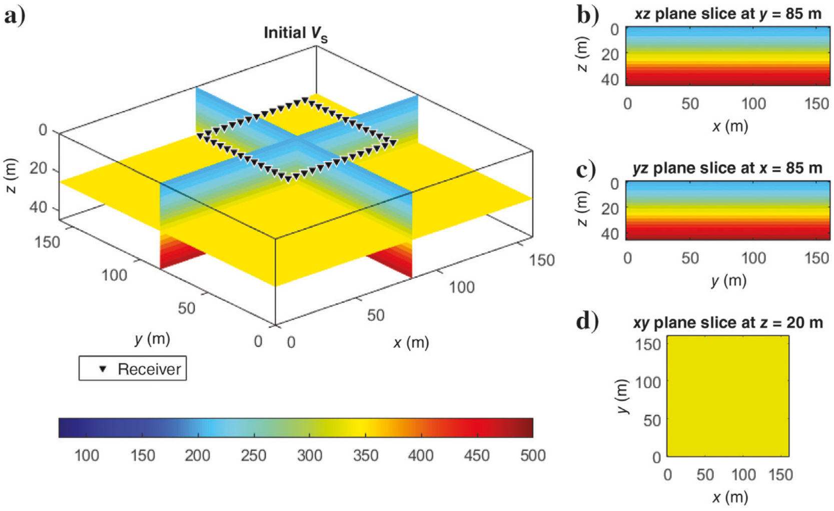

Figure 4. The initial V_S model used for the inversion of the synthetic example. (a) Black triangles represent the receivers on the array's boundary (note that 196 receivers are evenly distributed within this boundary on a 5 m grid — not shown). (b) The *xz* plane slice at $y = 85$ m, (c) *yz* plane slice at $x = 85$ m, and (d) *xy* plane slice at $z = 20$ m.

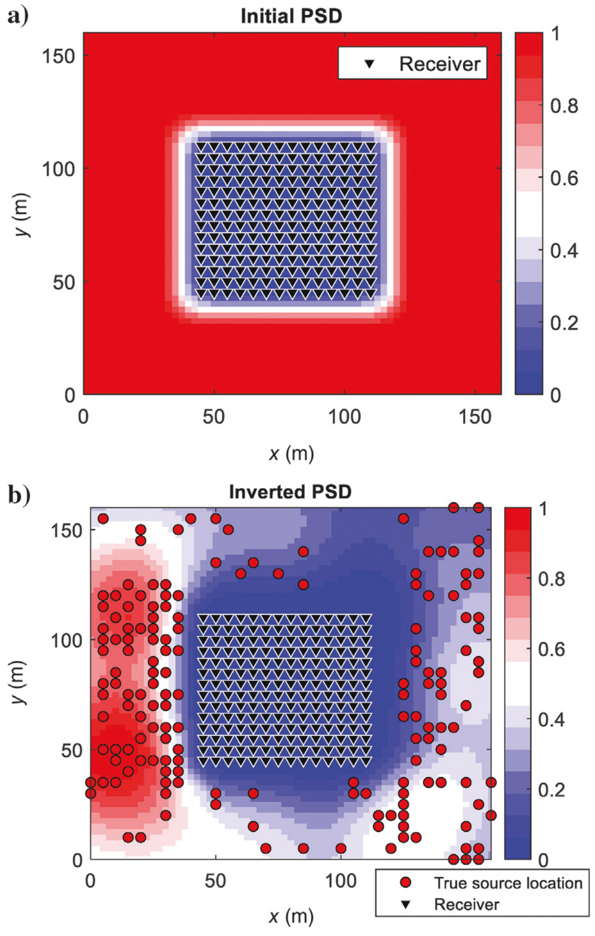

Figure 5. The PSD inversion for the synthetic example. (a) The initial assumed PSD. (b) The final inverted PSD. Red circles represent the true locations of the noise sources.

advantage of inverting the PSD is that individual source locations are not required for analysis, making it applicable to field data in which the individual source locations cannot be determined.

The inverted V_S is shown in Figure 6. As a reminder, the true V_S model is shown in Figure 1. The low-velocity anomaly is characterized by the estimated location and size close to the ground truth. The center of this inverted anomaly is located at 18 m, which is slightly shallower than the ground truth of 20 m. Most model updates took place within the receiver-covered area (50–100 m in the *x*- and *y*-directions). The background V_S model outside of the array does not change significantly during the inversion, which means that the initial model is sufficiently accurate for the inversion to converge.

Figure 7 shows the 1D vertical V_S profiles at the center of the low-V_S anomaly ($x = 80$ m, $y = 80$ m) for the true, initial, and inverted models. The inverted V_S profile is close to the true model, with a minor difference in depth. This difference could be caused by the difference in the deep background V_S between the true and initial models and the lack of low-frequency signals to cover the deep structure.

The observed and simulated CCFs are compared to evaluate the algorithm's effectiveness. The CCFs for a sample reference station (station 61) are shown in Figure 8. The CCFs are plotted in every other trace for better visualization. At the first iteration, the initial waveform peaks arrive earlier in the simulated (synthetic) CCF than in the observed CCF (e.g., at stations 100–196) This difference in arrival time is caused by the low-V_S anomaly in the true model that is not present in the inversion starting model and is more evident between receiver pairs with large offsets. At the final iteration, the waveform consistency between the observed and the simulated CFFs is drastically improved, and the traveltime difference becomes much smaller. The waveform comparison (Figure 8b) contains no apparent arrival-time misfit. The waveform misfit (e.g., at stations 160–190) is minor but still exists. This waveform misfit is a combined effect produced by errors in the source estimation, the PSD inversion, and the velocity structure inversion.

The misfit between the observed and simulated CCFs is shown in Figure 9, where the error is normalized by dividing the misfit after each iteration by the misfit of the first iteration. The error decreases rapidly during the first 20 iterations and more slowly for the remaining iterations. At the last iteration (no. 45), the final normalized error is approximately 0.6, which indicates that the inverted V_S model better explains the observed CCF.

FIELD EXPERIMENT

A field experiment was conducted at the GVDA test site (Figure 10) in California. The site is located in a seismically active region of southern California, approximately 115 km northeast of San Diego, 150 km southeast of Los Angeles, 7 km east of the San Jacinto Fault, and 35 km west of the San Andreas Fault (Teague et al., 2018). Invasive and noninvasive geotechnical site characterization efforts performed previously at the GVDA site include downhole seismic testing (Gibbs, 1989), P-S suspension

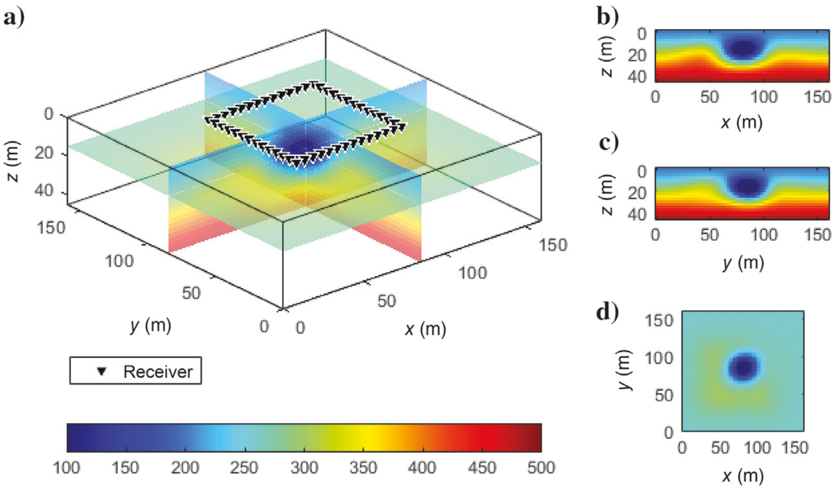

Figure 6. Final inversion results for the synthetic example. (a) The inverted 3D V_S model. Black triangles represent the receivers on the boundary of the sensor patch. (b) The xz plane slice at $y = 85$ m, (c) yz plane slice at $x = 85$ m, and (d) xy plane slice at $z = 20$ m.

logging (Steller, 1996), spectral analysis of surface waves (SASW) (Stokoe et al., 2004; Fathi et al., 2016), MASW and microtremor array measurements (MAMs) (Teague et al., 2018), and active-source FWI (Fathi et al., 2016). These investigations indicated that this site comprises 18–25 m of mostly sandy- to silty-sand alluvium (AL), overlaying decomposed granite (DG) that eventually transitions into unweathered granite at depths that vary between approximately 60 and 90 m across the site. The exact locations for some of these previous seismic tests are shown in Figure 10 relative to a large 2D sensor array used to collect data for this study.

We deployed an array of 196 3C 5 Hz nodal sensors on a 14 × 14 grid with 5 m spacing on the ground surface at GVDA. We recorded 28 h of ambient noises over two night-time deployments. The array's center (33.669°N, 116.673°W) is approximately 60 m to the southwest of a rural highway (the Pines to Palms highway). A 10 s example record of the recorded noise data is shown in Figure 11a. In this plot, seismograms are shown in the offset-time style. The offset is defined by the distance to reference station 1. A traffic-induced surface wave event can be identified from this plot between 3 and 4 s. This event traveled through the receiver area and leaves a trace of linear appearance in the seismogram.

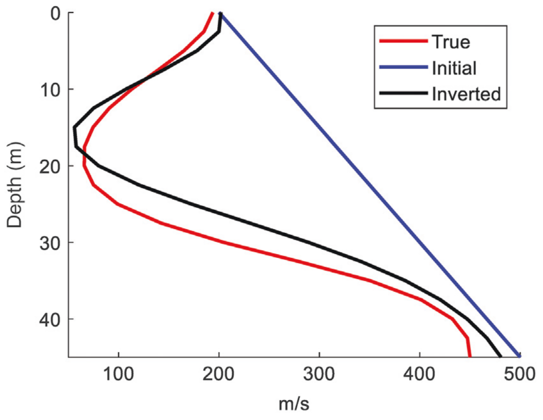

Figure 7. Comparison of the 1D V_S profiles at the center of the low-V_S anomaly ($x = 80$ m, $y = 80$ m) for the synthetic example.

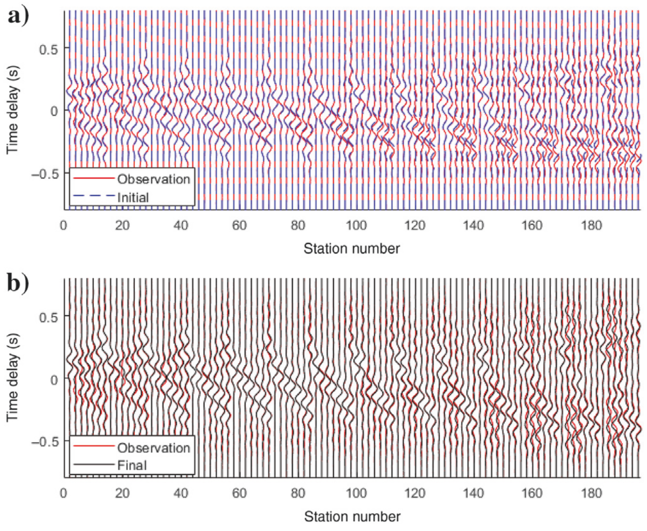

Figure 8. The CCF waveform comparisons relative to station 61 for the synthetic example at (a) the first iteration and (b) the final iteration. The CCFs are plotted every second trace for a better view.

The noise data CCF is computed and inverted following the same steps as those of the synthetic example. With the consistent noise energy from the traffic, we used the first 3 h of the recorded noise data to compute the CCFs. The rest of the data are typically redundant, as the CCFs are almost identical after adding later hours of the recorded data. The 3 h recorded data are filtered through 2–15 Hz bandwidth and divided into 1 s segments. The CCF between every station pair is calculated for each segment and sum over all segments. The CCFs between the individual stations and reference station 1 are shown in Figure 11b. Consistent waveforms are observed for most of the receiver pairs and clear arrivals can be identified for reference station 1, which is the closest to the highway (Figure 10).

For the inversion analysis, the velocity model is set as 160 m × 160 m × 45 m ($x \times y \times z$) and discretized into cells of 2.5 m × 2.5 m × 2.5 m. The receiver patch is near the model's center with the receiver x locations from 45 to 110 m and the receiver y locations from 35 to 100 m (Figure 12). This setting allows the modeled area to cover more than 100 m length of the highway close to the site, benefiting the noise source distribution estimation. Consulting the SASW and MASW results at the site (Fathi et al., 2016; Teague et al., 2018), we used a basic 1D initial model with V_S linearly increased from 180 m/s on the ground surface to 600 m/s at the model bottom (45 m depth). Similar to the synthetic experiment, the inversion was run for a total of 45 iterations and it took approximately 34 h on the same computer (32 cores of 3.46 GHz each and RAM of 1.0 TB). The inversion alternated between updating the PSD for five iterations and updating the models' V_S model for 10 iterations. During the inversion, V_P was updated as twice the value of V_S, and ρ was fixed to 1800 kg/m^3. It is noted that the V_P/V_S ratio is larger than two if the soil is below the ground water table (GWT), particularly for saturated clay (Brocher, 2005). Various V_P/V_S ratios can be used to update V_P to potentially improve the inverted V_S. However, due to the unknown GWT at the time of collecting the noise data and the low sensitivity of Rayleigh-wave-dominated CCFs to V_P, we updated the V_P as twice the value of V_S for general soils.

Figure 12 shows the inverted normalized PSD with a truncated (0–0.5) color scale used for better showing the noise source distribution. This result indicates that the ambient noise signals arrive from all directions (nonzero PSD), but mainly from the highway to the north. The signal power is especially strong along the shortest path from the road to the receiver array (Figure 10), indicating that traffic-induced surface waves dominate the recorded noise wavefield and the computed PSD is consistent with the noise sources.

The inverted 3D V_S model is shown in Figure 13. It shows softer materials with $V_S < \sim 250$ m/s over the top 10–20 m, which agrees quite well with the expected AL-DG layer interface, with rapidly increasing V_S at greater depths. The lateral variation of V_S is minimal, although the thickness of the softest near-surface material does vary significantly across the array. Due to the distribution of sensors and the PSD, the characterized area is mainly within the sensor array (45–110 m in the *x*-direction and 35–100 m in the *y*-direction). The initial model was updated very little outside of the sensor array.

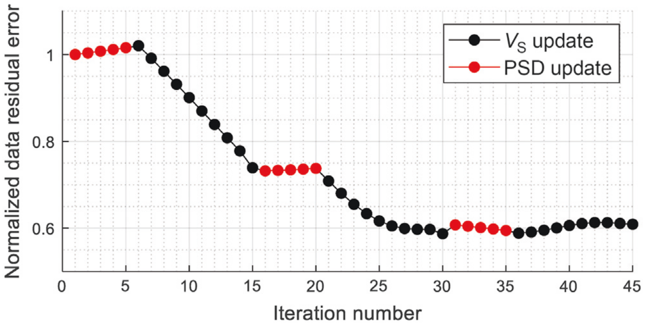

Figure 9. The normalized CCF misfit curve as a function of the inversion iteration for the synthetic example.

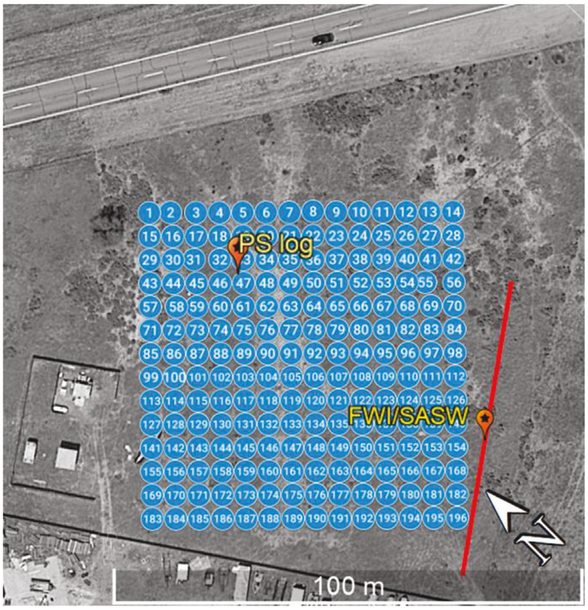

Figure 10. Plan view of the GVDA test site with the locations of several seismic testing (ANT, active-source FWI, and SASW) and PS log borehole. The blue circles represent the 196 3C 5 Hz nodal stations (this 3D ANT study), which were deployed in a 14 × 14 grid at a uniform spacing of 5 m.

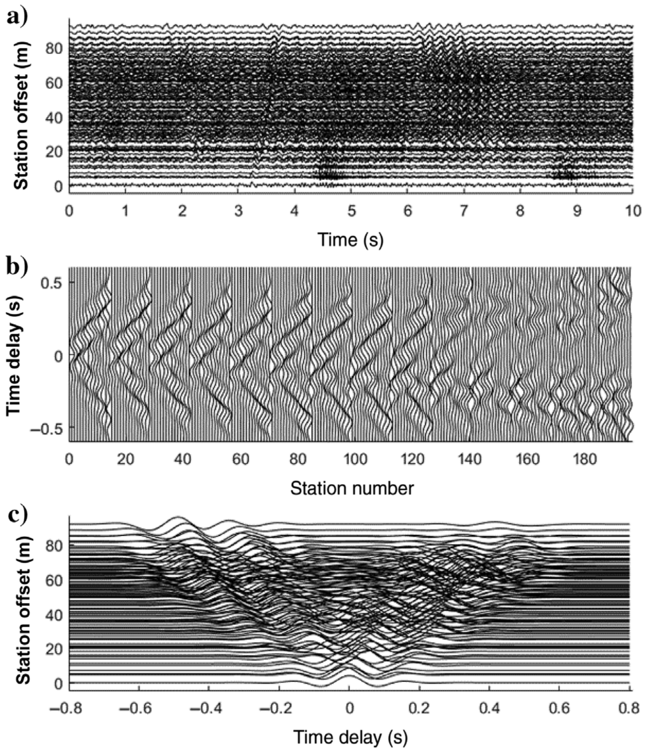

Figure 11. The GVDA experiment: (a) a sample of 10 s noise record, (b) computed CCFs displaced in time-sensor-number style, and (c) computed CCFs displaced in offset-time style. The CCFs are computed from 3 h of collected field data.

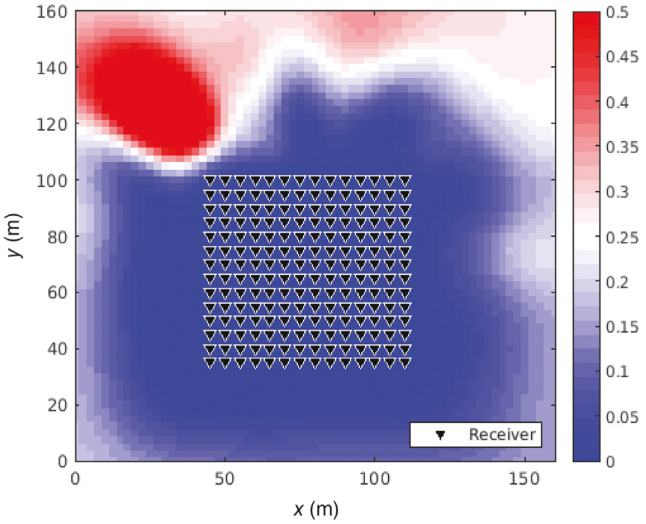

Figure 12. Inverted PSD for the GVDA data set. The black triangles represent the geophones.

To evaluate the 3D ANT algorithm's performance, we compare waveforms of the observed and simulated CCFs. The comparison is carried out for a sample reference station (station 61) near the boring log. At this station, the largest station offset is approximately 65 m (i.e., the distance to station 196). At the first iteration (Figure 14a), there is an evident gap in arrival times between the observed and simulated CCFs. This difference in the arrival times indicates that the field subsurface has an S-wave velocity slower than the initial model. This time difference is less evident with small station offsets (less than 30 m), implying that the initial model is more accurate in shallow depths. At the final iteration, the waveform match is significantly improved, and the arrival-time difference is small between the observed and simulated CCFs (Figure 14b).

Figure 15 shows the waveform comparison for 21 receiver pairs. The reference receivers (first receiver) are selected at every 10 stations, and the paired receivers (second receiver) are randomly selected. The offsets of these receiver pairs vary from 10 to 64 m (Table 1). The simulated CCF waveforms from the initial model are either faster than the observation or have waveforms significantly different from the observation. At the end of the 3D ANT inversion, the final simulated CCFs fit the observed CCFs reasonably well. The waveform misfit still exists after the final iteration, mostly due to the errors of source signal estimation, source PSD estimation, and V_S update. Nevertheless, the final waveform match is considered to be very good for uncontrolled-source seismic techniques (with unknown source locations and signatures).

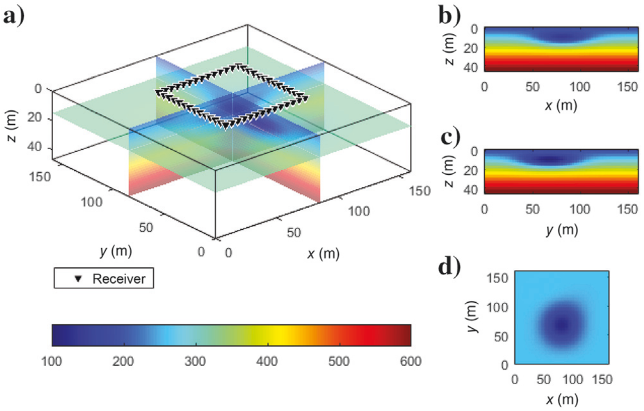

Figure 13. Inverted 3D V_S model for the GVDA data set. (a) The final inverted V_S model. Black triangles represent the receivers on the boundary of the sensor patch. (b) The xz plane slice at $y = 85$ m, (c) yz plane slice at $x = 85$ m, and (d) xy plane slice at $z = 20$ m.

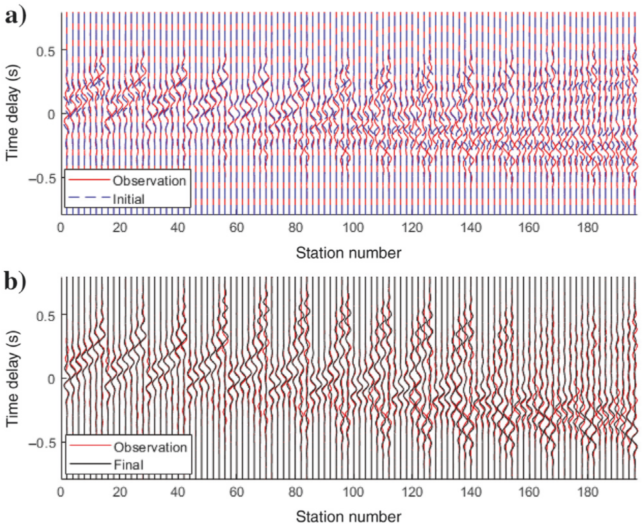

Figure 14. The CCF waveform comparisons relative to station 61 for the GVDA data set after (a) the first inversion iteration and (b) the last inversion iteration. The CCFs are plotted every second trace for a better view.

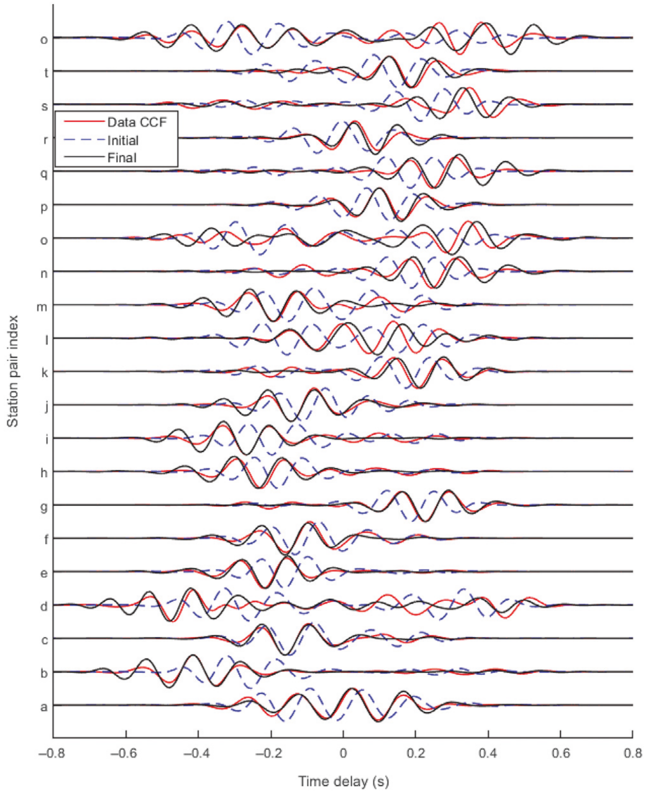

Figure 15. Sample CCF waveform comparisons for 21 receiver pairs across the GVDA receiver array. The first receivers are selected at every 10 stations, and the second receivers are randomly selected as provided in Table 1.

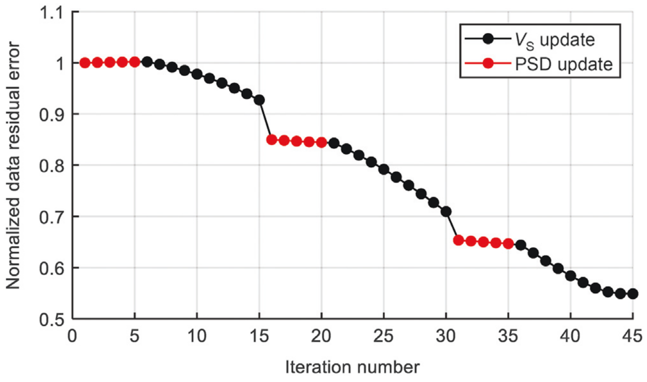

Figure 16. The normalized error versus inversion iterations for the GVDA data set.

The normalized least-squares error (i.e., misfit) is shown in Figure 16. The error gradually decreases to approximately 40% from the first to the final iterations, indicating that the final V_S model explains the data much better than the initial model. The error jumps at iterations 16 and 31 are mostly due to overfitting the CCFs by updating V_S at previous iterations, based on the current PSD. As the PSD and V_S updates are typically coupled, an accurate estimation of V_S requires a sufficient PSD and vice versa. The overfitting reduces the error, but it may not produce an accurate V_S update because the current PSD may not be a good estimation. After the PSD is corrected (updated), the error decreases further, suggesting that the strategy of independently updating the PSD and V_S iteratively can minimize the waveform misfit.

Table 1. Receiver pairs and offsets for traces shown in Figure 15.

Trace index	Reference station (first receiver)	Paired station (second receiver)	Offset (m)
a	1	62	32.0
b	10	174	63.2
c	20	29	25.4
d	30	178	64.0
e	40	121	33.5
f	50	74	22.3
g	60	10	36.0
h	70	120	36.0
i	80	173	43.0
j	90	146	20.0
k	100	64	33.5
l	110	49	32.0
m	120	157	29.1
n	130	51	39.0
o	140	48	50.0
p	150	96	22.3
q	160	50	41.2
r	170	142	10.0
s	180	38	50.9
t	190	123	29.1
o	196	89	57.0

The first receivers are selected at every 10 stations and the second receivers are randomly selected.

As noted previously, Steller (1996) performs P-S suspension logging (PS logging) at the GVDA site near station 47 ($x = 65$ m, $y = 85$ m; refer to Figure 10). To compare the 3D ANT results to the ground truth, we compare the initial V_S model, the inverted V_S model, and the simplified PS log data at the borehole's location (Figure 17a). The inverted V_S has good alignment with the PS logging data above 15 m and correctly reflects the increasing trend of V_S with depth. The AL-DG interface is estimated at approximately 18 m in the 3D ANT result, which is slightly deeper than that from the borehole PS logging data. This is likely due to the smoothness of the 3D ANT result and the resulting lack of reflected waves at the layer interface. Nevertheless, it shows the correct trend of velocity increment with depth.

Fathi et al. (2016) perform SASW and active-source FWI at this site. Figure 17b shows the comparison of 1D V_S profiles from the 3D ANT at a point near station 154 ($x = 110$ m, $y = 50$ m; refer to Figure 10) to those of SASW (line 1) and active FWI (at $x = 0$ m in Figure 15 of Fathi et al., 2016). The active FWI study provides accurate V_S profiles that agree with the SASW at depths above 10 m. However, the active FWI fails to characterize the AL-DG layer interface and the layer below 15 m depth, most likely due to the lack of low-frequency signals (2–5 Hz) used in the analysis. In contrast, the ANT inverted profile is more consistent with the SASW and PS logging results. The ANT and SASW produce similar results because both methods use low-frequency components (2–10 Hz) to image the deeper structure. Finally, it is noted that although the presented ANT method can provide greater imaging depths than active seismic methods, it currently does not allow for as great of profiling depths as possible with passive 1D profiling methods such as MAMs or SPAC.

CONCLUSION

This paper presents a new 3D ANT method, which analyzes noise CCFs for the characterization of 3D V_S subsurface structures at engineering scales (<50 m depth). The method does not require energy balance along directions of receiver pairs or far-field wavefields for GF retrieval. Instead, by accounting for noise source distribution directly, it inverts the full-waveform CCF for V_S structures. The method's capability is first demonstrated on a realistic synthetic example with the accurate characterization of the buried velocity anomaly. It is then tested on a large noise data set collected at the GVDA test site in southern California. The inverted noise source distribution is consistent with the known ambient sources (a nearby highway) and the inverted V_S model is consistent with prior invasive and noninvasive geotechnical site characterization data. Based on the synthetic and field experimental results, the ANT method is a useful geophysical tool for the characterization of 3D soil and rock profiles.

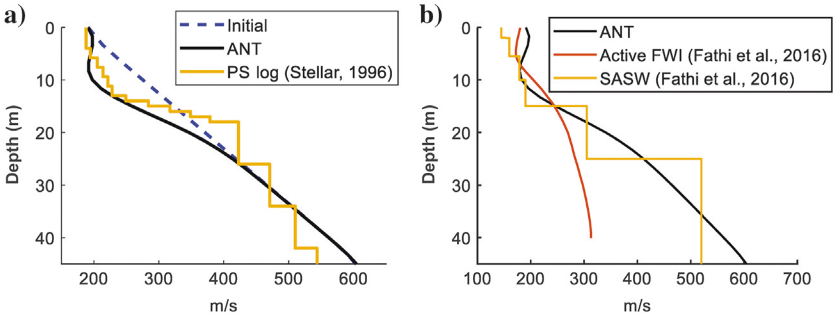

Figure 17. Comparison of 1D V_S profiles from the presented 3D ANT and those obtained previously at the GVDA site: (a) 3D ANT V_S profile at $x = 65$ m, $y = 85$ m in comparison to the PS logging V_S profile and (b) 3D ANT V_S profile at $x = 110$ m, $y = 50$ m in comparison to nearby SASW and active FWI V_S profiles.

ACKNOWLEDGMENTS

This work was supported by the National Science Foundation (grant nos. CMMI-1930697 and CMMI-1931162). However, any opinions, findings, conclusions, or recommendations expressed in this material are those of the authors and do not necessarily reflect the views of the National Science Foundation.

DATA AND MATERIALS AVAILABILITY

Data associated with this research are available and can be obtained by contacting the corresponding author.

REFERENCES

Aki, K., 1957, Space and time spectra of stationary stochastic waves, with special reference to microtremors: Bulletin of the Earthquake Research Institute, **35**, 415–456.

Alam, M. I., 2019, Near-surface characterization using traveltime and full-waveform inversion with vertical and horizontal component seismic data: Interpretation, **7**, no. 1, T141–T154, doi: 10.1190/INT-2018-0132.1.

Alam, M. I., and K. Shukla, 2020, P-wave velocity modeling for shallow subsurface characterization using full waveform inversion while comparing two different approaches of data processing for ground roll suppression: Geophysical Prospecting, **68**, 2078–2093, doi: 10.1111/1365-2478.12987.

Asten, M. W., N. Lam, G. Gibson, and J. Wilson, 2002, Microtremor survey design optimised for application to site amplification and resonance modelling: Total risk management in the privatised era, *in* M. Griffith, D. Love, P. McBean, A. McDougall, and B. Butler, eds., Proceedings of Conference, Australian Earthquake Engineering Society, Paper 7.

Barmin, M. P., M. H. Ritzwoller, and A. L. Levshin, 2001, A fast and reliable method for surface wave tomography, *in* A. L. Levshin and M. H. Ritzwoller, eds., Monitoring the comprehensive nuclear-test-ban treaty: Surface waves: Springer, 1351–1375.

Behm, M., N. Nakata, and G. Bokelmann, 2016, Regional ambient noise tomography in the Eastern Alps of Europe: Pure and Applied Geophysics, **173**, 2813–2840, doi: 10.1007/s00024-016-1314-z.

Brocher, T. M., 2005, Empirical relations between elastic wave speeds and density in the earth's crust: Bulletin of the Seismological Society of America, **95**, 2081–2092, doi: 10.1785/0120050077.

Capon, J., 1969, High-resolution frequency-wavenumber spectrum analysis: Proceedings of the IEEE, **57**, 1408–1418, doi: 10.1109/PROC.1969.7278.

Cho, I., T. Tada, and Y. Shinozaki, 2004, A new method to determine phase velocities of Rayleigh waves from microseisms: Geophysics, **69**, 1535–1551, doi: 10.1190/1.1836827.

Cox, B. R., and A. N. Beekman, 2011, Intramethod variability in ReMi dispersion measurements and V_S estimates at shallow bedrock sites: Journal of Geotechnical and Geoenvironmental Engineering, **137**, 354–362, doi: 10.1061/(ASCE)GT.1943-5606.0000436.

Cox, B. R., and D. P. Teague, 2016, Layering ratios: A systematic approach to the inversion of surface wave data in the absence of a priori information: Geophysical Journal International, **207**, 422–438, doi: 10.1093/gji/ggw282.

Das, R., and S. S. Rai, 2016, Seismic interferometry and ambient noise tomography: Theoretical background and application in south India: Journal of Physics: Conference Series, **759**, 012006, doi: 10.1088/1742-6596/759/1/012006.

De Ridder, S. A. L., and J. R. Maddison, 2018, Full wavefield inversion of ambient seismic noise: Geophysical Journal International, **215**, 1215–1230, doi: 10.1093/gji/ggy328.

Di Giulio, G., C. Cornou, M. Ohrnberger, M. Wathelet, and A. Rovelli, 2006, Deriving wavefield characteristics and shear-velocity profiles from two-dimensional small-aperture arrays analysis of ambient vibrations in a small-size alluvial basin, Colfiorito, Italy: Bulletin of the Seismological Society of America, **96**, 1915–1933, doi: 10.1785/0120060119.

Ekström, G., G. A. Abers, and S. C. Webb, 2009, Determination of surface-wave phase velocities across USArray from noise and Aki's spectral formulation: Geophysical Research Letters, **36**, L18301, doi: 10.1029/2009GL039131.

Endrun, B., M. Ohrnberger, and A. Savvaidis, 2010, On the repeatability and consistency of three-component ambient vibration array measurements: Bulletin of Earthquake Engineering, **8**, 535–570, doi: 10.1007/s10518-009-9159-9.

Fang, L., J. Wu, Z. Ding, and G. F. Panza, 2010, High resolution Rayleigh wave group velocity tomography in North China from ambient seismic noise: Geophysical Journal International, **181**, 1171–1182, doi: 10.1111/j.1365-246X.2010.04571.x.

Fathi, A., B. Poursartip, K. H. Stokoe, and L. Kallivokas, 2016, Three-dimensional P-and S-wave velocity profiling of geotechnical sites using full-waveform inversion driven by field data: Soil Dynamics and Earthquake Engineering, **87**, 63–81.

Foti, S., F. Hollender, F. Garofalo, D. Albarello, M. Asten, P.-Y. Bard, C. Comina, C. Cornou, B. Cox, and G. Di Giulio, 2018, Guidelines for the good practice of surface wave analysis: A product of the InterPACIFIC project: Bulletin of Earthquake Engineering, **16**, 2367–2420, doi: 10.1007/s10518-017-0206-7.

Gibbs, J. F., 1989, Near-surface P- and S-wave velocities from borehole measurements near Lake Hemet, California, U.S. Geological Survey Open File Report.

Guo, Z., X. Gao, H. Yao, J. Li, and W. Wang, 2009, Midcrustal low-velocity layer beneath the central Himalaya and southern Tibet revealed by ambient noise array tomography: Geochemistry, Geophysics, Geosystems, **10**, Q05007, doi: 10.1029/2009GC002458.

Hayashi, K., M. Asten, W. Stephenson, C. Cornou, M. Hobiger, M. Pilz, and H. Yamanaka, 2022, Microtremor array method using SPAC analysis of Rayleigh-wave data: Journal of Seismology, **26**, 601–627, doi: 10.1007/s10950-021-10051-y.

Henstridge, J. D., 1979, A signal processing method for circular arrays: Geophysics, **44**, 179–184, doi: 10.1190/1.1440959.

Johnson, D. H., and D. E. Dudgeon, 1993, Array signal processing: Concepts and techniques: PTR Prentice-Hall Inc.

Lacoss, R. T., E. J. Kelly, and M. N. Toksöz, 1969, Estimation of seismic noise structure using arrays: Geophysics, **34**, 21–38, doi: 10.1190/1.1439995.

Lin, F.-C., D. Li, R. W. Clayton, and D. Hollis, 2013, High-resolution 3D shallow crustal structure in Long Beach, California: Application of ambient noise tomography on a dense seismic array: Geophysics, **78**, no. 4, Q45–Q56, doi: 10.1190/geo2012-0453.1.

Lin, F.-C., M. H. Ritzwoller, and R. Snieder, 2009, Eikonal tomography: Surface wave tomography by phase front tracking across a regional broad-band seismic array: Geophysical Journal International, **177**, 1091–1110, doi: 10.1111/j.1365-246X.2009.04105.x.

Louie, J. N., 2001, Faster, better: Shear-wave velocity to 100 meters depth from refraction microtremor arrays: Bulletin of the Seismological Society of America, **91**, 347–364, doi: 10.1785/0120000098.

Mirzanejad, M., K. T. Tran, M. McVay, D. Horhota, and S. Wasman, 2020, Sinkhole detection with 3D full seismic waveform tomography: Geophysics, **85**, no. 5, B147–B157, doi: 10.1190/geo2019-0490.1.

Mirzanejad, M., K. T. Tran, M. McVay, D. Horhota, and S. Wasman, 2021, Deep void detection with 3D full waveform inversion of surface-based and in-depth source seismic wavefields: Engineering Geology, **294**, 106407, doi: 10.1016/j.enggeo.2021.106407.

Moschetti, M. P., M. H. Ritzwoller, F. Lin, and Y. Yang, 2010, Seismic evidence for widespread western-US deep-crustal deformation caused by extension: Nature, **464**, 885–889, doi: 10.1038/nature08951.

Nguyen, T. D., and K. T. Tran, 2018, Site characterization with 3D elastic full-waveform tomography: Geophysics, **83**, no. 5, R389–R400, doi: 10.1190/geo2017-0571.1.

Nolet, G., and G. F. Panza, 1976, Array analysis of seismic surface waves: Limits and possibilities: Pure and Applied Geophysics, **114**, 775–790, doi: 10.1007/BF00875787.

Okada, H., 2003, The microtremor survey method: SEG, Geophysical Monograph Series 12.

Park, C. B., R. D. Miller, and J. Xia, 1999, Multichannel analysis of surface waves: Geophysics, **64**, 800–808, doi: 10.1190/1.1444590.

Ritzwoller, M. H., F.-C. Lin, and W. Shen, 2011, Ambient noise tomography with a large seismic array: Comptes Rendus Geoscience, **343**, 558–570, doi: 10.1016/j.crte.2011.03.007.

Rosenblad, B. L., and J. Li, 2009, Comparative study of refraction microtremor (ReMi) and active source methods for developing low-frequency surface wave dispersion curves: Journal of Environmental & Engineering Geophysics, **14**, 101–113, doi: 10.2113/JEEG14.3.101.

Sager, K., C. Boehm, L. Ermert, L. Krischer, and A. Fichtner, 2020, Global-scale full-waveform ambient noise inversion: Journal of Geophysical Research: Solid Earth, **125**, e2019JB018644, doi: 10.1029/2019JB018644.

Sager, K., L. Ermert, C. Boehm, and A. Fichtner, 2018, Towards full waveform ambient noise inversion: Geophysical Journal International, **212**, 566–590, doi: 10.1093/gji/ggx429.

Schippkus, S., D. Zigone, G. Bokelmann, and A. W. Group, 2018, Ambient-noise tomography of the wider Vienna Basin region: Geophysical Journal International, **215**, 102–117, doi: 10.1093/gji/ggy259.

Steller, R., 1996, New borehole geophysical results at GVDA, UCSB Internal Report, http://nees.ucsb.edu/gvdageodata/GVDA-Geotech-Stellar1996.pdf.

Stokoe, K. H., A. Kutulus, and F. Y. Menq, 2004, SASW measurements at the NEES Garner Valley test site, California, University of Texas at Austin, College of Engineering Data Report.

Teague, D. P., B. R. Cox, and E. M. Rathje, 2018, Measured vs. predicted site response at the Garner Valley Downhole Array considering shear wave velocity uncertainty from borehole and surface wave methods: Soil Dynamics and Earthquake Engineering, **113**, 339–355, doi: 10.1016/j.soildyn.2018.05.031.

Tokimatsu, K., 1997, Geotechnical site characterization using surface waves: Proceedings of the IS-Tokyo'95, The First International Conference on Earthquake Geotechnical Engineering.

Tran, K. T., M. McVay, M. Faraone, and D. Horhota, 2013, Sinkhole detection using 2D full seismic waveform tomography: Geophysics, **78**, no. 5, R175–R183, doi: 10.1190/geo2013-0063.1.

Tran, K. T., and J. Sperry, 2018, Application of 2D full-waveform tomography on land-streamer data for assessment of roadway subsidence: Geophysics, **83**, no. 3, EN1–EN11, doi: 10.1190/geo2016-0550.1.

Tromp, J., Y. Luo, S. Hanasoge, and D. Peter, 2010, Noise cross-correlation sensitivity kernels: Geophysical Journal International, **183**, 791–819, doi: 10.1111/j.1365-246X.2010.04721.x.

Vantassel, J., B. Cox, L. Wotherspoon, and A. Stolte, 2018, Mapping depth to bedrock, shear stiffness, and fundamental site period at Centreport, Wellington, using surface-wave methods: Implications for local seismic site amplification: Bulletin of the Seismological Society of America, **108**, 1709–1721, doi: 10.1785/0120170287.

Wang, Y., K. T. Tran, and D. Horhota, 2021, Road sinkhole detection with 2D ambient noise tomography: Geophysics, **86**, no. 6, KS123–KS135, doi: 10.1190/geo2020-0739.1.

Wapenaar, K., 2004, Retrieving the elastodynamic Green's function of an arbitrary inhomogeneous medium by cross correlation: Physical Review Letters, **93**, 254301, doi: 10.1103/PhysRevLett.93.254301.

Wapenaar, K., and J. Fokkema, 2006, Green's function representations for seismic interferometry: Geophysics, **71**, no. 4, SI33–SI46, doi: 10.1190/1.2213955.

Xia, J., R. D. Miller, and C. B. Park, 1999, Estimation of near-surface shear-wave velocity by inversion of Rayleigh waves: Geophysics, **64**, 691–700, doi: 10.1190/1.1444578.

Yang, Y., M. H. Ritzwoller, and C. H. Jones, 2011, Crustal structure determined from ambient noise tomography near the magmatic centers of the Coso region, southeastern California: Geochemistry, Geophysics, Geosystems, **12**, Q02009, doi: 10.1029/2010GC003362.

Zheng, X., W. Jiao, C. Zhang, and L. Wang, 2010, Short-period Rayleigh-wave group velocity tomography through ambient noise cross-correlation in Xinjiang, Northwest China: Bulletin of the Seismological Society of America, **100**, 1350–1355, doi: 10.1785/0120090225.

Biographies and photographs of the authors are not available.